Noname manuscript No.
(will be inserted by the editor)

Dielectric and Double Debye Parameters of Artificial Normal Skin and Melanoma

Rui Zhang [1] · **Ke Yang**[2] · **Bin Yang**[3,4] · **Najah Abed AbuAli**[5] · **Mohammad Hayajneh** [5] · **Mike Philpott**[6] · **Qammer H. Abbasi**[7] · **Akram Alomainy**[1]

Received: date / Accepted: date

Abstract The aim of this study is to characterise the artificial normal skin and melanoma by testing samples with different fibroblast and metastatic melanoma cell densities using Terahertz (THz)-Time Domain Spectroscopy (TDS) Attenuated Total Reflection (ATR) technique. Results show that melanoma samples have higher refractive index and absorption coefficient than artificial normal skin with the same fibroblast density in the frequency range between 0.4 and 1.6 THz, and this contrast increases with frequency. It is primarily because that the melanoma samples have higher water content than artificial normal skin, and the main reason to melanoma containing more water is that tumour cells degrade the contraction of the collagen lattice. In addition, complex refractive index and permittivity of the melanoma samples have larger variations than that of normal skin samples. For example, the refractive index of artificial normal skin at 0.5 THz increases 4.3% while that of melanoma samples increases 8.7% when the cell density rises from 0.1 M/ml to 1 M/ml. It indicates that cellular response of fibroblast and melanoma cells to THz radiation is significantly different. Furthermore, the extracted Double Debye (DD) model parameters demonstrate that the static permittivity at low frequency and slow relaxation time can be reliable classifiers to differentiate melanoma from healthy skin regardless of the cell density. This study helps understand

Najah Abed AbuAli
E-mail: najah@uaeu.ac.ae
Rui Zhang
E-mail: rui.zhang@bit.edu.cn
[1]Department of Information and Electronic, Beijing Institute of Technology, Beijing, China
[2]School of Marine Science and Technology, Northwestern Polytechnical University, Xi'an, China
[3] Electronics and Electrical Engineering, University of Chester, Chester, UK
[4] Beijing Advanced Innovation Center for Imaging Technology, Department of Physics, Capital Normal University, Beijing, China
[5] College of Information Technology, United Arab Emirates University, Al-Ain, UAE
[6] Centre for Cell Biology and Cutaneous, Queen Mary University of London, London, UK
[7] School of Engineering, University of Glasgow, Glasgow, UK

the complex response of skin tissues to THz radiation and the origin of the contrast between normal skin and cancerous tissues.

Keywords THz-TDS ATR · Dielectric properties · Double Debye model · Artificial skin · Melanoma

1 Introduction

Early detection of the cancer, and thus to prevent further penetration of cancerous cells into deeper layers and enable early treatment such as surgical excision is key to eradicating the disease [1]. The traditional cancer diagnosis depends on evaluating the clinical examination of biopsy specimens to explore the histopathological details of the patient. Although the biopsy is considered as a gold standard for diagnosis, it may be time-consuming, expensive, and cause pain for patients [2]. Thus, it is imperative to develop diagnostic medical imaging techniques for non-invasively detecting cancerous cells and mapping the tumour margin. Due to the THz radiation is non-ionised to biological tissues and highly sensitive to water content, THz pulse-based techniques have significant applications in biomedical field. THz technology as a tool to detect the tumour has been widely studied, especially for the breast cancer [3], skin cancer [4, 5], liver cancer [6]. THz technology could be a more effective cancer diagnosis tool than other conventional medical imaging modalities because the tumour and healthy tissues have different responses to THz radiation.

When it comes to skin cancer, common types of skin cancer are divided into two categories: cutaneous malignant melanoma and non-melanoma skin cancer (NMSC) [7]. NMSC is the most prevalent skin cancer in the light-skinned population, and it includes basal cell carcinoma (BCC) and squamous cell carcinoma (SCC). Malignant melanoma is one common skin cancer that begins in the melanocytes, and it occurs among all adequately studied racial and ethnic groups. Melanoma is dangerous because it is much more likely to spread to other parts of the body if not caught early.

Since last decade, an increasing number of studies have been conducted on the characterisation of the healthy and malignant human tissues in the THz frequencies. The potentiality for THz pulsed spectroscopy usage for diagnostics of BCC was shown in works [4, 8, 9]. It has been validated that changes in absorption coefficient and refractive index are important factors explaining the contrast in skin cancer and normal skin. The origin of the contrast between healthy and diseased tissues in the THz frequencies was initially focused on the changes in water content [4, 10, 11]. But it was not clear what brings this difference in water content. In the further exploration of the source mechanism for the contrast, it was found that water content variation is not the only cause of contrast in some studies [6, 12]. The structural changes in the cells were responsible in part for the changes in the THz optical properties between healthy and cirrhotic liver tissues [6]. THz imaging at $-20°C$ shows better contrast between the cancer tissue and normal mucosa than the room temperature THz imaging at 20 $°C$ in the frequency domain [13]. It

was regarded that the THz distinction between normal and cancerous tissues originated from cellular structure deformation, as confirmed by histological analysis, because the effect of water in blood could be removed by freezing tissues before taking THz measurements. Apart from BCC, attention is also paid on melanoma skin cancer. The THz dielectric characteristics of healthy skin, dysplastic and non-dysplastic skin nevi were shown in [14,15]. It demonstrated that the dysplastic nevi, as precursors of melanoma, could be identified by the difference in the complex permittivities from healthy skin. But the origin of the difference was not further explored.

Above research are all conducted with real diseased tissues. The biological tissue is a very complex system from the chemical, physical, and biological point of view. Each of the basic components of water, tissue-lipids, fat collagen, epithelial cell cytoplasm *etc.* represents a complex chemical composition and structure. It is therefore essential to characterise the structure and composition at all levels to understand the complex response of such tissues to THz radiation. The characterisation of artificial tissues with controllable compositions and variations can be an alternative approach to further explore the different response to THz radiation between healthy and cancerous tissues. A preliminary investigation was carried out on artificial normal skin and melanoma skin cancer in [16]. In this paper, the study is extended to more samples with three different fibroblast and melanoma cell densities, and comprehensive analysis on the material properties is presented.

The Double Debye (DD) model is targeted for the mechanism of interaction between THz radiation and water molecules [17]. Due to the high water proportion of skin as well as increased water content of skin tumour compared to normal skin, DD model was used to describe the dielectric spectra of skin, both cancerous and healthy in [5,11,18]. The DD model is also considered as a promising component for the discrimination between healthy and diseased tissues. The experiment carried out on BCC, both ex-vivo and in-vivo, shows that there are significant differences in extracted DD parameters between normal and BCC tissues, hence suggesting their potential for the cancer discrimination. The fitting algorithm as well as optimisation of the extraction of the DD parameters were improved in [18, 19]. With utilisation of the updated fitting algorithm, the classification capability of the DD parameters to discriminate between BCC and normal skin was also confirmed and it was found that the best classifier was the static permittivity at low frequency of DD parameters in [20]. In this paper, the DD model is applied to describe the dielectric response of artificial normal skin and melanoma to THz radiation, which helps understand the contrast mechanism of healthy and cancerous tissues.

The knowledge of skin structure and constituent is necessary for the investigation on artificial skin and melanoma. Skin can be divided into three main layers: epidermis, dermis and subcutaneous fat. Dermis the thickest layer. In normal human skin, melanocytes are aligned at the basement membrane, separating the epidermis from dermis as shown in Fig. 1. In this work, the investigation is carried out with WM1158, which is a highly aggressive melanoma cell line with mesenchymal morphology. Different from normal melanocytes,

WM1158 melanoma cells invade into the dermis layer [21]. In synthetic biology, dermal equivalent (DE) is developed by seeding dermal fibroblast cells in collagen gel to progressively re-organise the lattice [22]. DE has been used as a replacement for human skin in various fields of skin biology [23]. The collagen lattice is contracted and water is squeezed out in the contraction process. Specifically, it has been shown that DE contracts more at high fibroblasts concentration and low collagen concentration [22]. The impact of cell density and collagen concentration on the electromagnetic properties of DE in the THz Band has been experimentally studied and presented in [24]. More importantly. in general, the collagen concentration and the number of cells determine the rate of contraction, but some categories of cells have a reduced capacity to contract lattices, namely, transformed cells, tumour cells, established cell lines [25]. The findings on tumour cells degrading collagen contraction motivate the study to quantify the difference in THz electromagnetic parameters between artificial normal skin tissues and melanoma with different cell densities.

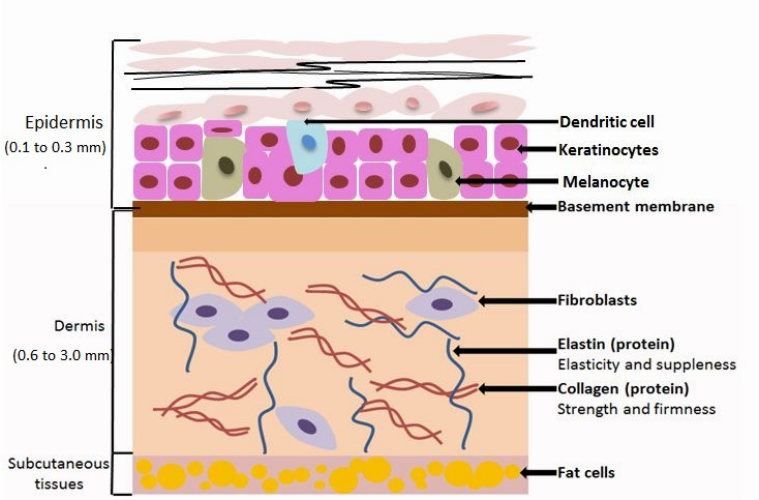

Fig. 1 Schematic of human skin structure and constituent cell types. Skin is stratified composed of the epidermis, dermis and subcutaneous fat. The dermis is the thickest layer, which is mainly comprised of collagen and fibroblasts. Melanocytes are aligned at the basement membrane, separating the epidermis from dermis [23].

In this work, three duplicate artificial normal skin and melanoma samples with different fibroblast and melanoma cell densities were prepared and five repeatable measurements were conducted at the same spot of each sample by using THz-TDS ATR technique. It alleviates the uncertainty caused by sample thickness and generates statistical information of the samples, which enables the extraction of optical parameters with high accuracy. Apart from the comparison in complex refractive index, complex permittivites are calculated

to evaluate the deviations between the artificial normal skin and melanoma. The DD model is applied to characterise the frequency-dependent dielectric response of THz radiation to tissues and the extraction optimisation problem are presented. The extracted DD model parameters are compared to strengthen their potentiality to discriminate the melanoma from normal skin tissues, and the findings on the variations on these parameters are analysed.

2 Sample Preparation and Methods

2.1 Sample Preparation

Aforementioned, human skin fibroblasts cultured in a hydrated lattice of type I collagen appears to be a substitute for normal living dermis. Collagen provides scaffolding, nutrient delivery, and potential for cell-to-cell interaction. The standard collagen mixture is made up in the following parts: type I collagen makes up 8 parts of final mix, 10X Minimum Essential Medium (MEM) makes 1 part and Fetal Bovine Serum (FBS) containing the desired number of fibroblast cells makes 1 part. Collagen lattices were made with a final collagen concentration of 2 mg/ml. The reason for choosing this concentration is that the THz parameters of artificial skin with such collagen are closer to the real skin as demonstrated in [24, 26]. The collagen lattices were cast in 12-well plastic dishes with 1.5 ml mixture per well.

In the normal skin tissue-like samples, 1 Million (M)/ ml fibroblast cells solely were seeded in collagen solution and incubated for gelation at 37 $^{\circ}C$, 5% CO_2 for approximately 15 minutes. While in the melanoma samples, 0.5 M/ml fibroblast were cast in collagen solution to allow gel; After gelling, 0.5 M/ml WM1158 melanoma cells suspended in 1 ml RPMI (Roswell Park Memorial Institute) medium were inoculated on the top of the fibroblast-populated collagen gels. Then incubate the samples in the incubator at 37 $^{\circ}C$, 5% CO_2 and change the medium every day. After 5 days incubation, THz measurement was conducted on the samples with THz-TDS ATR system. Another two comparative sets with different cell densities were prepared as shown in the Table. 1, in order to study the relations of the melanoma cell density and the THz optical parameters of the artificial samples. The selection of the cell densities is in line with literature [21, 27].

Table 1 Artificial normal skin and melanoma samples with different fibroblast and melanoma cell densities.

Sample number	Cell constituent
S1 (normal)	1 M/ml Fibroblast cells
S2 (melanoma)	0.5 M/ml Fibroblast cells+ 0.5 M/ml Melanoma cells
S3 (normal)	0.5 M/ml Fibroblast cells
S4 (melanoma)	0.25 M/ml Fibroblast cells+ 0.25 M/ml Melanoma cells
S5 (normal)	0.1 M/ml Fibroblast cells
S6 (melanoma)	0.05 M/ml Fibroblast cells+ 0.05 M/ml Melanoma cells

Fig. 2 are digital images of artificial normal skin sample 1 and melanoma sample 2 on the third day after gelling simultaneously. It is observed that, at the same moment, the artificial melanoma sample has larger surface area than the artificial normal skin sample, which reflects that melanoma sample contracts more slowly. This phenomenon happens to other comparative sets of samples. The main reason is that melanoma cells degrade the contraction of collagen lattice as demonstrated in [25].

(a) Artificial normal skin (b) Artificial melanoma

Fig. 2 Top down digital photographs of an artificial (a) normal skin sample 1 with 1 M/ml fibroblast cells and (b) melanoma sample 2 with 0.5 M/ml fibroblast cells + 0.5 M/ml melanoma cells. It is observed that the melanoma sample contracts more slowly than the normal sample.

2.2 Attenuated Total Reflection

Because the THz radiation is largely attenuated by the biological tissues with high water content, samples are required to be thin enough to enable acceptable intensity come to the detector in THz-TDS operating in the transmission mode. It brings much complexity in the sample preparation, sample thickness determination and experiment operation. To overcome the difficulty, geometry of the reflection measurement is well optimised to obtain accurate optical parameters of aqueous bio-molecular mediums. THz-TDS ATR is one of the reflection techniques that have been explored. It has been confirmed that THz-TDS ATR technique is suitable for measuring samples with high absorbance [28, 29].

With the major advantages in faster sampling, excellent sample-to-sample reproducibility and minimal operator-induced variations, THz-TDS ATR provides excellent data quality together with high reproducibility for highly absorbing samples. The core element of a THz-TDS ATR system is a prism,

and usually the prism is made of silicon which is almost transparent and non-disperive across the THz frequencies [30]. In the ATR technique, the THz beam from the emitter is directed into a silicon prism of relatively higher refractive index. The THz wave reflects from the prisms internal surface and produces an evanescent wave, which projects orthogonally into the sample in close contact with the ATR prism. The sample absorbs some of the energy of the evanescent wave and the reflected radiation (some now absorbed by the sample) is returned to the detector. The single reflection THz-TDS ATR phenomenon is graphically depicted in Fig. 3.

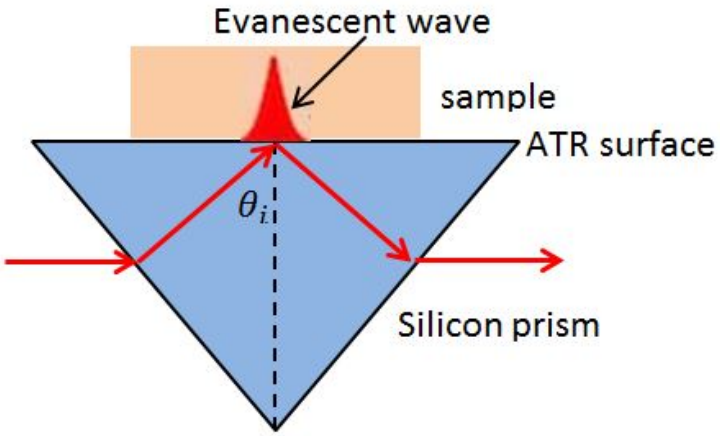

Fig. 3 Graphical representation of a single reflection THz-TDS ATR.

The depth of penetration d_p of the THz beam into the sample depends on the wavelength, the refractive indices of the ATR crystal and the sample and the angle of the entering light beam. Technically, d_p is defined as the distance required for the electric field amplitude to fall to e^{-1} of its value at the surface and is further defined by the well-known equation,

$$d_p = \frac{\lambda}{2\pi(\sqrt{n_1^2 sin_\theta^2 - n_2^2})} \tag{1}$$

where λ represents the wavelength of light and θ is the angle of incidence of the THz beam relative to a perpendicular from the surface of the crystal. It is typically of the order of a few microns (5 -40 μm) in the frequency band of interest.

In order to achieve a high quality spectrum, it is necessary to ensure good contact between the sample and ATR prism as the evanescent wave penetrates only up to a specific number of microns into the sample. Moreover, dry nitrogen is purged to remove water vapour. The sample thickness is ensured to be greater than the penetration depth of the evanescent field.

In ATR spectroscopy, the temporal waveforms of a sample and a reference are obtained. The ratio of the reflected complex amplitude of the sample to the reference is [31],

$$\frac{R_{sam}}{R_{ref}} = Pe^{-i\Delta} \tag{2}$$

where R_{sam} and R_{ref} are the Fast Fourier Transform (FFT) complex amplitude reflected at the ATR surface with and without sample, respectively. P refers to the absolute value of the ratio, while Δ denotes the phase shift.

According to [31], the squared complex refractive index of the sample, $\widetilde{n}^2$ is expressed as,

$$\widetilde{n}^2 = \frac{sin^2\theta_i(1-\sqrt{1-4(sin\theta_{sam}cos\theta_{sam})^2})}{2(sin\theta_{sam}cos\theta_{sam})^2} n_{Si}^2 \tag{3}$$

where θ_{sam} is the transmission angle with sample and n_{Si} is the refractive index of the silicon. Here, the refractive index of silicon n_{Si} is 3.41 and the incident angle θ_i is 51.5°. Based on the extracted $\widetilde{n}^2$, the real and imaginary parts of the refractive index can be calculated.

3 Double Debye Model

The Double Debye model is characterised by the frequency-dependent dielectric function as [5, 32, 33],

$$\epsilon_r(\omega) = \epsilon_\infty + \frac{\epsilon_s - \epsilon_2}{1+j\omega\tau_1} + \frac{\epsilon_s - \epsilon_\infty}{1+j\omega\tau_2} \tag{4}$$

where ϵ_∞ is the limiting permittivity at high frequency in the real part, which is a superposition of higher frequency resonances such as intra-molecular vibration modes and electron excitation [34]. The second and third terms are the slow and fast relaxation mode, respectively. Relaxation is a reactive process that may involve translational and rotational diffusion, hydrogen bond rearrangement, and structural rearrangement depending on the time scale. Such processes will be associated with activation energies and may have a significant temperature dependence. It is suggested that the molecules of liquid water are in the form of tetrahedral structure. When water is excited by the incident THz radiation, the structure is perturbed and reorients; the structure must break to enable this to happen. Thus, four hydrogen bonds need to be broken, which is a slow process τ_1. Subsequently, the single water molecule will reorient and move to a new tetrahedral site, which is a fast process τ_2 [35, 36]. Two relaxation times indicate the size of the coupling between the relaxation mode and the electric field. ϵ_s is the static permittivity at low frequency, and ϵ_2 is the intermediate dielectric constant for the description of the transitional state between the two relaxation processes [35]. $\epsilon_s - \epsilon_2$ and $\epsilon_s - \epsilon_\infty$ refer to the dispersion in amplitude of the slow and fast relaxation processes, respectively.

The numerical value of the frequency-dependent complex permittivity $\epsilon_r^m(\omega)$ is obtained by,

$$\epsilon_r^m(\omega) = (n(\omega) - j\frac{c\alpha(\omega)}{2\omega})^2 \tag{5}$$

where $n(\omega)$ and $\alpha(\omega)$ are the measured frequency-dependent refractive index and absorption coefficient, respectively.

The standard squared error between the relative complex permittivity $\epsilon_r(\omega)$ and its actual value $\epsilon_r^m(\omega)$ at a frequency sample ω_i is,

$$\begin{aligned} E(\omega_i) &= |\epsilon_r(\omega) - \epsilon_r^m(\omega)|^2 \\ &= |\epsilon_\infty + \frac{\epsilon_s - \epsilon_2}{1 + j\omega\tau_1} + \frac{\epsilon_s - \epsilon_\infty}{1 + j\omega\tau_2} - \epsilon_r^m(\omega)|^2 \end{aligned} \tag{6}$$

In fitting the complex permittivity with its DD model, the sum of the squared residuals is minimised. Accordingly, the five DD parameters ϵ_s, ϵ_2, ϵ_∞, τ_1 and τ_2 in Eq. 4 are extracted from the following total square error minimisation,

$$\begin{aligned} &\min_{\epsilon_s,\epsilon_2,\epsilon_\infty,\tau_1,\tau_2} \sum_{i=1}^{N} E(\omega_i) \\ \text{subject to} \quad &\epsilon_\infty \geq \epsilon_0, \epsilon_s \geq \epsilon_2, \epsilon_2 \geq \epsilon_\infty \\ &\tau_1 \geq 0, \tau_2 \geq 0 \end{aligned} \tag{7}$$

where N is the number of data points used to fit the model over the frequency range 0.4 to 1.6 THz.

The Particle Swarm Optimisation (PSO) was used to extract the DD model parameters of the collagen samples, which shown that the proposed dielectric model matches well with the dielectric properties of collagen not only at the high range of frequency (beyond 1 THz) but also at the lower band in [37]. Therefore, PSO algorithm [38] is also implemented in this work. The number of particles chosen in the PSO algorithm is 100 and this algorithm ends after 1000 iterations if the threshold is not reached before the optima.

4 Data Analysis

4.1 Complex Refractive Index

The obtained averaged values of refractive index and absorption coefficient of duplicate artificial normal skin and melanoma samples with three different cell densities are presented in Fig. 4. It is shown that the refractive index and absorption coefficient of melanoma are higher than artificial normal skin tissues with the same fibroblast cell density in the frequency band between 0.4 and 1.6 THz. In addition, the difference increases with the frequency, which indicates better contrast in higher frequency (beyond 1 THz). It is mainly because that

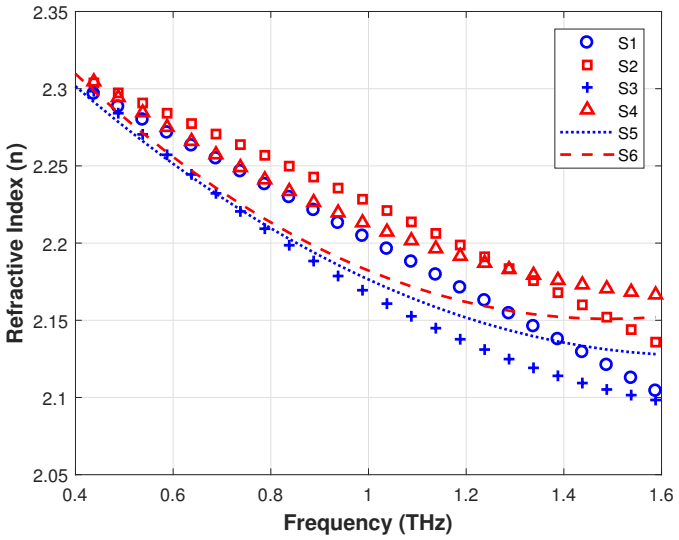

(a) Refractive index

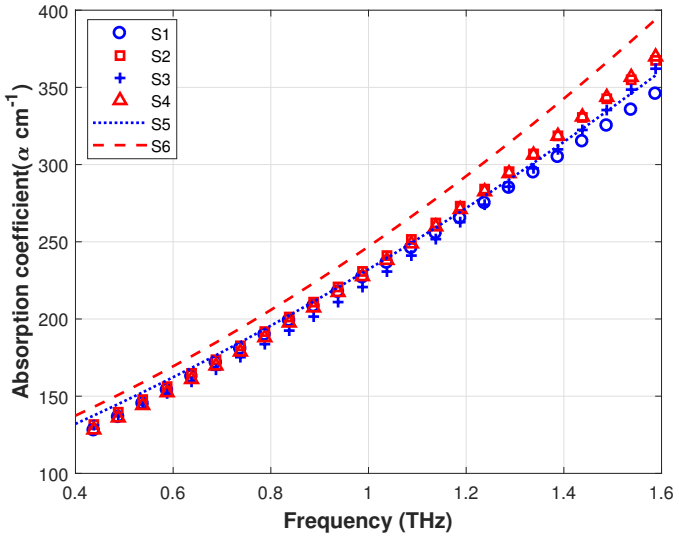

(b) Absorption coefficient

Fig. 4 The measured (a) refractive indexes and (b) absorption coefficients of six types of samples as listed in Table .1.

tumours in general have increased water content, which agrees with the findings in the studies using positron emission tomography and nuclear magnetic resonance techniques [39,40]. Moreover, the reason for increased water content is mainly that tumour cells have a reduced capacity to contract lattices [41].

It means that less water is squeezed out from the melanoma samples in the lattice contraction process, causing melanoma having higher water content left than normal samples. Besides, THz radiation has a higher sensitivity to water content at higher frequencies in the THz band.

4.2 Permittivity

As optical properties are directly related to dielectric permittivities, a concrete understanding of dielectric properties of the tissues provides a deeper insight into the contrast mechanism between normal and cancerous tissues. Based on the mean values of the measured complex refractive index above, the complex permittivity can be calculated to characterise the artificial tissues. The extracted permittivity and fitted values using PSO algorithm for six types of samples are shown in Fig. 5. Although there is no consistent difference in the real part, it is observed that the melanoma samples have higher imaginary permittivities than the normal skin samples for all kinds of cell densities. This difference is getting larger with the rise of the frequency. Therefore, the imaginary permittivity could be adopted as a reliable classifier to differentiate artificial melanoma from normal skin.

4.3 The Impact of Cell Density

The impact of the cell density on the contrast between the material parameters of the artificial normal and melanoma tissues has been studied. The measured mean and standard deviations of complex refractive index and permittivity of artificial normal skin and melanoma samples from multiple measurement are shown in Fig. 6 as a function of cell density at 0.5 THz.

It is observed that there is a standard deviation of around 0.01 to 0.04 in refractive index, about 2 cm^{-1} to 20 cm^{-1} in absorption coefficient and 0.2 in both real and imaginary permittivity of the samples with three kinds of cell densities. These differences of the same sample could be generated by the uncertainty in, such as leftovers around the samples, flatness of the sample and slight difference in cell numbers and cell states in the collagen mixture.

Moreover, the complex refractive index parameters of melanoma samples have larger variations than that of normal skin samples. For example, the refractive index of artificial normal skin at 0.5 THz increases 4.3% while that of melanoma samples increases 8.7% with the cell density rises from 0.1 M/ml to 1 M/ml. The absorption coefficient of the melanoma samples deceases from 153 cm^{-1} to 138 cm^{-1} when the cell density increases from 0.1 M/ml to 0.5 M/ml and then increase to 142 cm^{-1} when the cell density rises to 1 M/ml, which is more sharp than the variation in artificial normal skin from 147 cm^{-1} to 139 cm^{-1} and then to 138 cm^{-1}. It is also shown that both real and imaginary permittivities of melanoma samples change more sharply than normal samples with cell density. The larger variations in both refractive

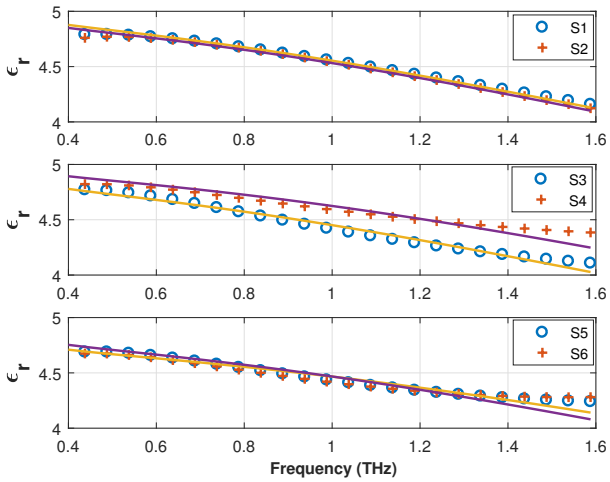

(a) Real Permittivity

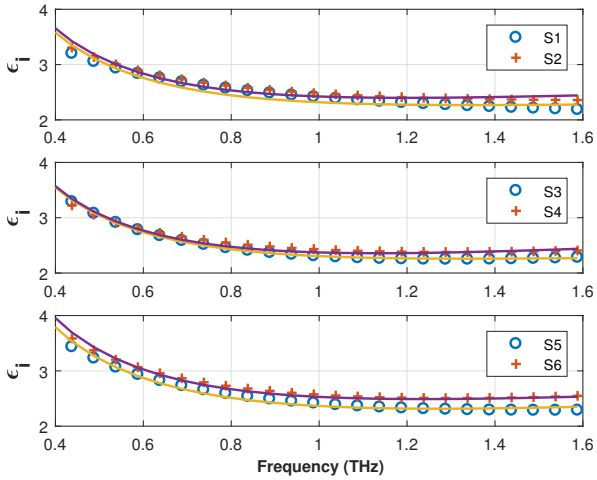

(b) Imaginary Permittivity

Fig. 5 The measured average complex permittivities of artificial normal skin and melanoma samples as listed in Table. 1 and their fitting models with yellow line referring to the normal sample while purple line denoting melanoma.

index and permittivity of melanoma samples indicate that cellular response of fibroblast and melanoma cells to pulsed THz radiation can be significantly different.

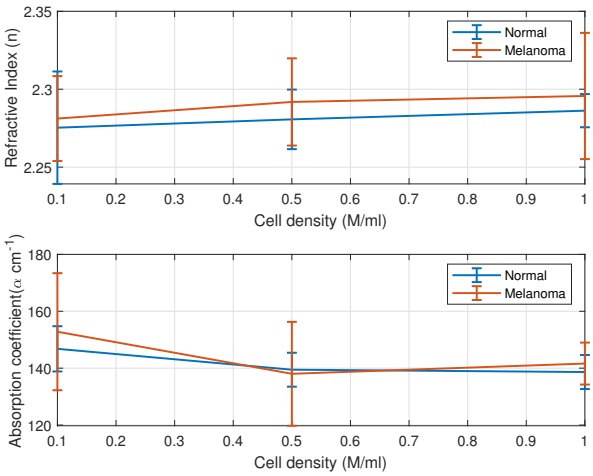

(a) Complex refractive index

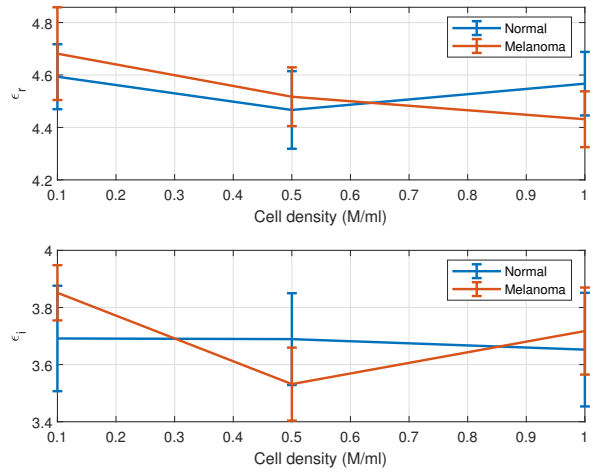

(b) Complex permittivity

Fig. 6 The measured average and standard deviation of (a) absorption coefficient and refractive index (b) real and imaginary permittivity of artificial normal skin and melanoma changes with cell density at 0.5 THz.

4.4 Double Debye Model Parameters

With the utilisation of PSO algorithm, the fitted permittivities of the various samples are obtained as illustrated in Fig. 5. The model is well fitted with the measured results. In addition, the extracted DD model parameters with mean and standard deviations for six categories of tissues are listed in Table.

Table 2 Double Debye parameters of artificial normal skin and melanoma samples with different fibroblast and melanoma cell densities determined from the particle swarm optimisation method.

Samples	ϵ_s	ϵ_2	ϵ_∞	$\tau_1(ps)$	$\tau_2(ps)$
S1 (normal)	24.976(1.535)	4.650(0.001)	4.557(0.141)	3.936(0.024)	0.486(0.004)
S2 (melanoma)	47.228(4.165)	4.746(0.098)	4.669(0.125)	4.910(0.042)	0.47(0.027)
S3 (normal)	33.370(2.140)	4.460(0.001)	4.412(0.116)	3.931(0.004)	0.489(0.002)
S4 (melanoma)	53.360(2.376)	4.621(0.001)	4.489(0.098)	4.982(0.001)	0.488(0.002)
S5 (normal)	33.890(1.916)	4.460(0.001)	4.489(0.116)	3.930(0.004)	0.488(0.003)
S6 (melanoma)	58.371(1.349)	4.622(0.001)	4.343(0.125)	4.983(0.001)	0.488(0.001)

2. It is seen that the static dielectric constant ϵ_s of melanoma samples are higher than the artificial normal skin samples. More specifically, ϵ_s of artificial normal skin sample 1 is 24.976, while that of melanoma sample 2 increases to approximately 47.228. The one in the second comparison between normal sample 3 and melanoma sample 4 increases from 33.370 to 53.360, while it rises from 33.890 in normal sample 5 to 58.371 in melanoma sample 6.

Additionally, it is observed that slow relaxation time τ_1 in melanoma samples is longer than artificial normal skin samples of all three sets of comparison. For instance, slow relaxation time of the normal sample 1 is 3.936 while it is 4.910 in the melanoma sample 2. It is apparent that there is a strong correlation between the cell type and density and the DD model parameters. These findings also confirm the capability of DD model parameters to differentiate the melanoma from the normal skin tissues.

5 Conclusions

This work introduces a promising approach by varying the composition and concentration of cells in artificial tissues to characterise the different response to the THz radiation between normal and cancerous tissues. The obtained results show that over the frequency range 0.4 to 1.6 THz, the melanoma samples have higher refractive indexes and absorption coefficients than artificial normal skin samples. It is mainly because that tumour cells have a reduced capacity to contract collagen lattices, causing melanoma samples contain more water. The refractive index and permittivity of melanoma samples has larger variations than the normal skin samples, indicating that cellular response of fibroblast and melanoma cells to pulsed THz radiation is significantly different. Besides the water content, the cell type and density is relevant with the structure of tissues, which in turn changes the THz electromagnetic parameters of artificial tissues. Multi-parameter approach can be adopted including permittivity and DD parameters to classify melanoma from healthy tissue. The static permittivity at low frequency and slow relaxation time of DD model parameters are confirmed as good classifiers to differentiate the artificial normal skin from melanoma. These findings in this paper provide a better understanding of the THz response to healthy and cancerous tissues and introduce more informative features for cancer classification.

Acknowledgement

This work is funded by project # AARE17- 019 provided by the ADEC Award for Research Excellence, Abu Dhabi, United Arab Emirates University.

References

1. D.S. Rigel, J. Russak, R. Friedman, CA: a cancer journal for clinicians **60**(5), 301 (2010)
2. G.G. Hallock, D.A. Lutz, Plastic and reconstructive surgery **101**(5), 1255 (1998)
3. A.J. Fitzgerald, V.P. Wallace, M. Jimenez-Linan, L. Bobrow, R.J. Pye, A.D. Purushotham, D.D. Arnone, Radiology **239**(2), 533 (2006)
4. R.M. Woodward, B.E. Cole, V.P. Wallace, R.J. Pye, D.D. Arnone, E.H. Linfield, M. Pepper, Physics in Medicine & Biology **47**(21), 3853 (2002)
5. E. Pickwell, B. Cole, A. Fitzgerald, V. Wallace, M. Pepper, Applied Physics Letters **84**(12), 2190 (2004)
6. S. Sy, S. Huang, Y.X.J. Wang, J. Yu, A.T. Ahuja, Y.t. Zhang, E. Pickwell-MacPherson, Physics in medicine and biology **55**(24), 7587 (2010)
7. T. Diepgen, V. Mahler, British Journal of Dermatology **146**, 1 (2002)
8. V.P. Wallace, R.M. Woodward, A.J. Fitzgerald, E. Pickwell, R.J. Pye, D.D. Arnone, in *Lasers in Surgery: Advanced Characterization, Therapeutics, and Systems XIII*, vol. 4949 (International Society for Optics and Photonics, 2003), vol. 4949, pp. 353–360
9. M.A. Brun, F. Formanek, A. Yasuda, M. Sekine, N. Ando, Y. Eishii, Physics in Medicine & Biology **55**(16), 4615 (2010)
10. E. Pickwell, B. Cole, A. Fitzgerald, M. Pepper, V. Wallace, Physics in Medicine and Biology **49**(9), 1595 (2004)
11. V.P. Wallace, A.J. Fitzgerald, E. Pickwell, R.J. Pye, P.F. Taday, N. Flanagan, T. Ha, Applied spectroscopy **60**(10), 1127 (2006)
12. Y.C. Sim, J.Y. Park, K.M. Ahn, C. Park, J.H. Son, Biomedical optics express **4**(8), 1413 (2013)
13. Y.C. Sim, K.M. Ahn, J.Y. Park, C.S. Park, J.H. Son, IEEE Transactions on Terahertz Science and Technology **3**(4), 368 (2013)
14. K. Zaitsev, N. Chernomyrdin, K. Kudrin, I. Reshetov, S. Yurchenko, Optics and Spectroscopy **119**(3), 404 (2015)
15. K.I. Zaytsev, N.V. Chernomyrdin, K.G. Kudrin, A.A. Gavdush, P.A. Nosov, S.O. Yurchenko, I.V. Reshetov, in *Journal of Physics: Conference Series*, vol. 735 (IOP Publishing, 2016), vol. 735, pp. 012–076
16. R. Zhang, K. Yang, Q. Abbasi, N.A. AbuAli, A. Alomainy, in *2018 43rd International Conference on Infrared, Millimeter, and Terahertz Waves (IRMMW-THz)* (IEEE, 2018), pp. 1–2
17. C. Rønne, S.R. Keiding, Journal of Molecular Liquids **101**(1-3), 199 (2002)
18. B.C. Truong, H.D. Tuan, H.H. Kha, H.T. Nguyen, IEEE Transactions on Biomedical Engineering **60**(6), 1528 (2013)
19. B.C. Truong, H. Tuan, A.J. Fitzgerald, V.P. Wallace, H. Nguyen, in *2014 36th Annual International Conference of the IEEE Engineering in Medicine and Biology Society* (IEEE, 2014), pp. 718–721
20. B.C. Truong, H.D. Tuan, V.P. Wallace, A.J. Fitzgerald, H.T. Nguyen, IEEE Transactions on Terahertz Science and Technology **5**(6), 990 (2015)
21. P. Eves, C. Layton, S. Hedley, R. Dawson, M. Wagner, R. Morandini, G. Ghanem, S. Mac Neil, British journal of dermatology **142**(2), 210 (2000)
22. E. Bell, B. Ivarsson, C. Merrill, Proceedings of the National Academy of Sciences **76**(3), 1274 (1979)
23. F. Meier, M. Nesbit, M.Y. Hsu, B. Martin, P. Van Belle, D.E. Elder, G. Schaumburg-Lever, C. Garbe, T.M. Walz, P. Donatien, et al., The American journal of pathology **156**(1), 193 (2000)

24. R. Zhang, K. Yang, Q.H. Abbasi, N.A. AbuAli, A. Alomainy, IEEE Transactions on Terahertz Science and Technology **8**(99), 1 (2018)
25. K. Ross, R. Gordon, Journal of microscopy **128**(1), 7 (1982)
26. E. Berry, A.J. Fitzgerald, N.N. Zinov'ev, G.C. Walker, S. Homer-Vanniasinkam, C.D. Sudworth, R.E. Miles, J.M. Chamberlain, M.A. Smith, in *Medical Imaging 2003* (International Society for Optics and Photonics, 2003), pp. 459–470
27. F. Grinnell, C.R. Lamke, Journal of cell science **66**(1), 51 (1984)
28. H. Hirori, K. Yamashita, M. Nagai, K. Tanaka, Japanese journal of applied physics **43**(10A), L1287 (2004)
29. M. Nagai, H. Yada, T. Arikawa, K. Tanaka, International journal of infrared and millimeter waves **27**(4), 505 (2006)
30. D. Grischkowsky, S. Keiding, M. Van Exter, C. Fattinger, JOSA B **7**(10), 2006 (1990)
31. A. Nakanishi, Y. Kawada, T. Yasuda, K. Akiyama, H. Takahashi, Review of Scientific Instruments **83**(3), 033103 (2012)
32. R.M. Hill, Nature **275**(5676), 96 (1978)
33. J. Barthel, R. Buchner, Pure and Applied Chemistry **63**(10), 1473 (1991)
34. T. Arikawa, M. Nagai, K. Tanaka, Chemical Physics Letters **457**(1-3), 12 (2008)
35. C. Ro/nne, L. Thrane, P.O. Åstrand, A. Wallqvist, K.V. Mikkelsen, S.R. Keiding, The Journal of chemical physics **107**(14), 5319 (1997)
36. E. Pickwell, A.J. Fitzgerald, B.E. Cole, P.F. Taday, R.J. Pye, T. Ha, M. Pepper, V.P. Wallace, Journal of Biomedical Optics **10**(6), 064021 (2005)
37. K. Yang, N. Chopra, Q. Abbasi, K. Qaraqe, A. Alomainy, IEEE Access (2017)
38. J. Kennedy, in *Encyclopedia of machine learning* (Springer, 2011), pp. 760–766
39. M. Bruehlmeier, U. Roelcke, J. Missimer, P.A. Schubiger, et al., The Journal of Nuclear Medicine **44**(8), 1210 (2003)
40. J. Chen, H. Avram, L. Crooks, M. Arakawa, L. Kaufman, A. Brito, Radiology **184**(2), 427 (1992)
41. B.M. Steinberg, K. Smith, M. Colozzo, R. Pollack, The Journal of cell biology **87**(1), 304 (1980)